Engineering Fracture Mechanics 232 (2020) 107048

Contents lists available at ScienceDirect

Engineering Fracture Mechanics

journal homepage: www.elsevier.com/locate/engfracmech

Dynamic fracture of soda-lime glass plates studied using two modified Digital Gradient Sensing techniques

Chengyun Miao, Hareesh V. Tippur*

Department of Mechanical Engineering, Auburn University, AL 36849, USA

ARTICLE INFO

Keywords:
Fracture mechanics
Dynamic crack growth
Soda-lime silicate glass
Digital Gradient Sensing (DGS) method
Optical metrology

ABSTRACT

Two modified full-field Digital Gradient Sensing (DGS) methods of higher measurement sensitivity, *transmission-reflection* DGS (*tr*-DGS) and *double-transmission* DGS (*t2*-DGS), are extended in this work to examine their feasibility to study fast fracture events in soda-lime glass by measuring stress gradients. Full-field optical measurement of deformations and stresses in such high-stiffness and low-toughness brittle material is very challenging. Extremely high crack speeds (~1400 m/s), low failure strain ($\epsilon_f < 0.1\%$), and highly localized sub-micron scale deformations are among the challenges to overcome in this material system to succeed in this regard. The higher measurement sensitivity of *tr*-DGS and *t2*-DGS make them particularly suitable for studying transparent glasses and ceramics relative to previous versions of DGS method. These two new methods are demonstrated for studying dynamically growing cracks in soda-lime glass plates subjected to dynamic impact loading in a modified Hopkinson pressure bar device and ultrahigh-speed photography (1 million fps). Previously proposed *reflection* DGS (*r*-DGS) is also implemented to comparatively show the benefits of higher measurement sensitivity offered by *tr*-DGS and *t2*-DGS methods. The measured stress gradients are numerically integrated to estimate ($\sigma_{xx} + \sigma_{yy}$) stress fields around the crack tip vicinity. The optical measurements are also used to obtain fracture parameter histories of crack speed, stress intensity factors and energy release rates under mode-I conditions. The energy release rates increase rapidly when the crack speed approaches ~1400 m/s. The measured fracture parameters are also assessed using a complementary elasto-dynamic finite element model up to crack initiation. The agreement between measurements and simulations supports the feasibility of these two optical methods for studying dynamic fracture mechanics of this challenging material.

1. Introduction

Transparent glasses such as soda-lime silicate glass are prevalent in engineering structures due to high-stiffness, superior hardness, high compression strength characteristics with low-cost and sustainable attributes. Further, they can be laminated with tough polymer interlayers to form transparent armor structures; e.g., automotive windshields [1]. Understanding the ability of such a brittle material to bear load without cracking under impact loading conditions is critical.

Full-field optical methods are generally popular for studying dynamic fracture of materials. However, it is quite challenging to implement them to quantify deformations around a dynamically growing crack in high-stiffness and low-toughness brittle material such as soda-lime silicate glass. This is because the crack tip deformations in these brittle materials are very small (crack opening

* Corresponding author.
E-mail address: tippuhv@auburn.edu (H.V. Tippur).

https://doi.org/10.1016/j.engfracmech.2020.107048
Received 20 January 2020; Received in revised form 24 March 2020; Accepted 9 April 2020
Available online 15 April 2020
0013-7944/

displacement < 100 nm), and the crack speeds are very high (>1500 m/s). Hence, most of the existing research on dynamic fracture of brittle materials is based on videography of crack propagation using high-speed cameras with *ex-situ* postmortem fractography. Bourne *et al.* [2] applied high-speed photography to study dynamic impact on soda-lime glass, and observed compressive shock and release waves due to fracture in the glass plates. Park and Chen [3] studied dynamic crack propagation across an interface in layered glass plates, and concluded that crack penetration behavior depended on the interface thickness. McCauley *et al.* [4] conducted edge-on impact tests on glass coupled with ultrahigh-speed photography; they found that defects had a significant effect on the nucleation of cracks and influenced the damage front evolution. Swab *et al.* [5] performed static and dynamic compression tests on boron carbide and recorded the fracture process using high-speed camera. Some researchers also applied X-ray phase contrast imaging (XPCI), which has a much higher spatial resolution than visible light techniques, to visualize *in-situ* fracture mechanisms in brittle materials. Parab *et al.* [6] applied XPCI to study dynamic fracture mechanisms of spherical soda-lime glass particles subjected dynamic compression. Leong *et al.* [7] investigated dynamic fracture in brittle solids using XPCI, and observed that crack branching occurred when the crack velocity approached ~ 45% of the Rayleigh wave speed. However, all the research mentioned above are based on imaging of the specimens and none have measured the mechanical fields around the crack tip directly. Accordingly, the fracture parameters such as stress intensity factors and energy release rate were not quantified during crack growth.

There are other full-field optical methods, which have been utilized to measure displacement or stress fields around the crack tip in brittle materials subjected to dynamic impact. Photoelasticity was adopted by Dally to investigate dynamic fracture in a brittle polyester by measuring isochromatic fringe patterns around a growing crack tip and calculating stress intensity factors [8]. Tippur *et al.* [9] developed a shearing interferometry technique called Coherent Gradient Sensing (CGS), and utilized it to measure stress gradients around a dynamically growing crack in PMMA plates. In recent years, Digital Image Correlation (DIC) methods have become popular to study dynamic fracture mechanics of brittle materials. Zhang and Zhao [10] applied DIC with crack propagation gauge (CPG) to investigate loading rate effect on fracture mechanics of geomaterials; they point out that DIC measurements were not accurate in high strain rate tests due to the limitation of small failure strain of those brittle materials. Ju *et al.* [11] comparatively investigated the dynamic crack propagation in rock measured by DIC and CPG techniques. They found that it was difficult to precisely determine the location of a propagating crack tip using DIC. Therefore, different thresholds of normal strains were utilized in order to increase the accuracy of DIC measurements. Shannahan *et al.* [12] studied dynamic fracture behavior of MAX phase ternary carbides and nitrides using DIC. However, their measured fracture parameters are limited by the spatial and temporal resolutions of the high-speed camera, revealing the challenge of applying DIC to study dynamic fracture of a high stiffness brittle material. In recent years, a full-field optical method called Digital Gradient Sensing (DGS) that utilizes DIC but measures two orthogonal angular deflections of light rays caused by stresses in transparent materials [13] or out-of-plane deformations of reflective solids [14] has become available. Sundaram and Tippur [15] were the first to extend transmission DGS (*t*-DGS) to study dynamic fracture mechanics of soda-lime glass; they too pointed out difficulty of implementing traditional DIC to study dynamic fracture in soda-lime glass. In a follow on work, Dondeti and Tippur [16] reported a comparative study of dynamic fracture of soda-lime glass using photoelastcity, DIC and *t*-DGS and demonstrated the advantages of *t*-DGS over the other two techniques. However, to implement *t*-DGS successfully in soda-lime glass, they had to increase the so-called 'optical lever' significantly (to > 1 m) relative to the polymer counterparts [17] (20–30 mm) to amplify the effects of the stress fields around the crack tip. This also required that the camera be located at long distances (of ~ 4 m) from the specimen to achieve paraxial approximation. These requirements in turn introduced challenges such as insufficient light to expose the camera sensor during dynamic events and vibration isolation under quasi-static conditions. To circumvent such problems, Miao and Tippur [18] proposed two variants of DGS of higher measurement sensitivity suitable for studying high-stiffness and low-toughness transparent solids. The principle of the method was demonstrated by the authors on PMMA [18] and its feasibility to study the intended material system such as soda-lime glass is an obvious the next step and is reported in this research.

This paper is structured as follows: The working principles of the original and the two higher sensitivity DGS methods are introduced first. Then, experiments on dynamic impact loading leading to fast fracture in soda-lime glass plates utilizing the new DGS methods are discussed. Subsequently, the fracture parameters such as crack velocities, stress intensity factors and energy release rate are extracted from the optical measurements. Companion finite element simulations are performed to assess the measurements independently. Finally, the major results of this research are summarized.

2. Digital Gradient Sensing (DGS) methods

2.1. Reflection Digital Gradient Sensing (r-DGS)

A schematic of the experimental setup for *reflection* Digital Gradient Sensing (or *r*-DGS) to measure surface slopes is shown in Fig. 1. A digital camera is used to record random speckles on a target plane via the reflective specimen surface. To achieve this, the specimen and the target plate are placed perpendicular to each other, and the beam splitter is positioned at 45° relative to the specimen and target plates, respectively. The target is coated with random black and white spray painted speckles, and is illuminated uniformly using broad spectrum white light. The specimen surface is made reflective (Fig. 2(a)) using vapor deposition of aluminum film or using the film transfer technique [19]. (In Fig. 2, the front face of the specimen is towards to the camera and the target.) When the specimen is in the undeformed state, the gray scale at a generic point P on the target plate is recorded by a pixel of the camera sensor through point O on the reflective specimen. Thus recorded image at that time instant and/or load level is the reference image. After the specimen suffers deformation, say, due to the applied load, the gray scale at a neighboring point of P namely, Q on the target plate is photographed by the same pixel of the sensor through the same point O on the specimen surface. The corresponding image of the specimen in the deformed state is recorded next. The local orthogonal speckle displacements $\delta_{y:x}$ can be obtained by correlating

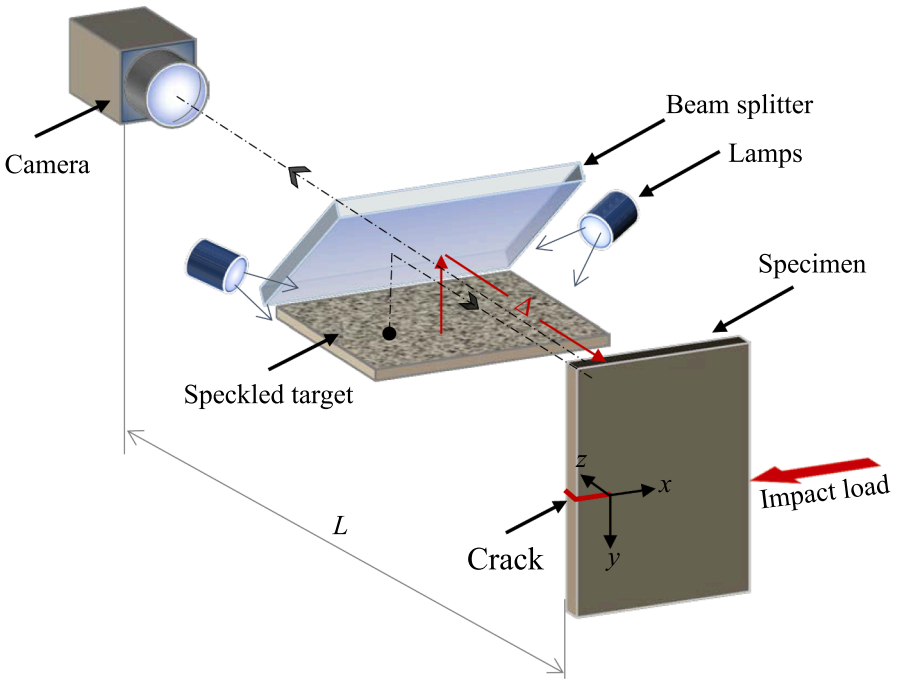

Fig. 1. Schematic of experimental setup for reflection DGS (*r*-DGS). (Setups for *t2*-DGS and *tr*-DGS are similar to *r*-DGS, see text for details).

images in the reference and deformed states. The corresponding angles $\phi_{y:x}$ representing two orthogonal angular deflections of light rays can then be obtained as shown in the schematic Fig. 3.

For simplicity, only the angular deflections of light rays in the *y*-*z* plane are shown in Fig. 3. Here, OP makes an angle ϕ_y with OQ. Further, $\phi_y = \theta_i + \theta_r$ where θ_i and $\theta_r(=\theta_i)$ are incident and reflected angles relative to the normal to the specimen. A similar relationship in the *x*-*z* plane can be obtained as well. Then, the two orthogonal surface slopes of the surface can be related to $\phi_{y:x}$ as $\frac{\partial w}{\partial y:x} = \frac{1}{2}\tan(\phi_{y:x})$. The governing equation for *r*-DGS thus is [14],

$$\frac{\partial w}{\partial y{:}\ x} = \frac{1}{2}tan(\phi_{y:x}) \approx \frac{1}{2}(\phi_{y:x}) \approx \frac{1}{2}\left(\frac{\delta_{y:x}}{\Delta}\right) = \left(-\frac{\upsilon B}{2E}\right)\frac{\partial(\sigma_{xx}+\sigma_{yy})}{\partial(y{:}\ x)} \tag{1}$$

where Δ is the distance or the gap between the specimen and target planes. It is important to note that the coordinates of the specimen plane are utilized for describing the governing equations and the camera is focused on the target plane during photography. Therefore, a coordinate mapping step is required to transfer the target plane locations to the specimen plane. This can be done by invoking the pin-hole camera approximation, $(x{:}\ y) = \frac{L}{L+\Delta}(x_0{:}\ y_0)$, where $(x{:}\ y)$ and $(x_0{:}\ y_0)$ represent the coordinates of the specimen and target planes, respectively, and *L* is the distance between the specimen and the camera [13].

2.2. Transmission Digital Gradient Sensing (t-DGS)

The working principles of *transmission* digital gradient sensing (*t*-DGS) are briefly introduced here for the sake of completeness, since *t2*-DGS and *tr*-DGS are based on modifications of *r*-DGS and *t*-DGS.

A schematic of the experimental setup for *t*-DGS method is shown in Fig. 4. Unlike in the *r*-DGS setup, a random speckle pattern on the target plate is recorded through a transparent specimen in *t*-DGS. As in *r*-DGS, a reference image is recorded first. That is, the gray level at point P on the target plane corresponding to point O on the specimen plane is recorded initially. The refractive index and thickness of the specimen change after imposing a load on the specimen. As a result, the light rays deviate from their initial path due to the so-called elasto-optical effect. In the deformed state of the specimen, another image is recorded with the gray scale at a neighboring point of P, namely Q, on the target plane, recorded by the same pixel through O on the specimen plane. The local orthogonal speckle displacements $\delta_{x:y}$ can be quantified by correlating the deformed image with the reference image of the specimen. The angles $\phi_{x:y}$ are the two orthogonal angular deflections of light rays, which are related to two orthogonal stress gradients. The governing equation for *t*-DGS is [13]:

$$(\phi_{y:x})_{t-DGS} = \frac{\delta_{y:x}}{\Delta} = C_\sigma B\frac{\partial(\sigma_{xx}+\sigma_{yy})}{\partial(y{:}\ x)} \tag{2}$$

where C_σ is the elasto-optic constant of the specimen material, *B* is the undeformed thickness.

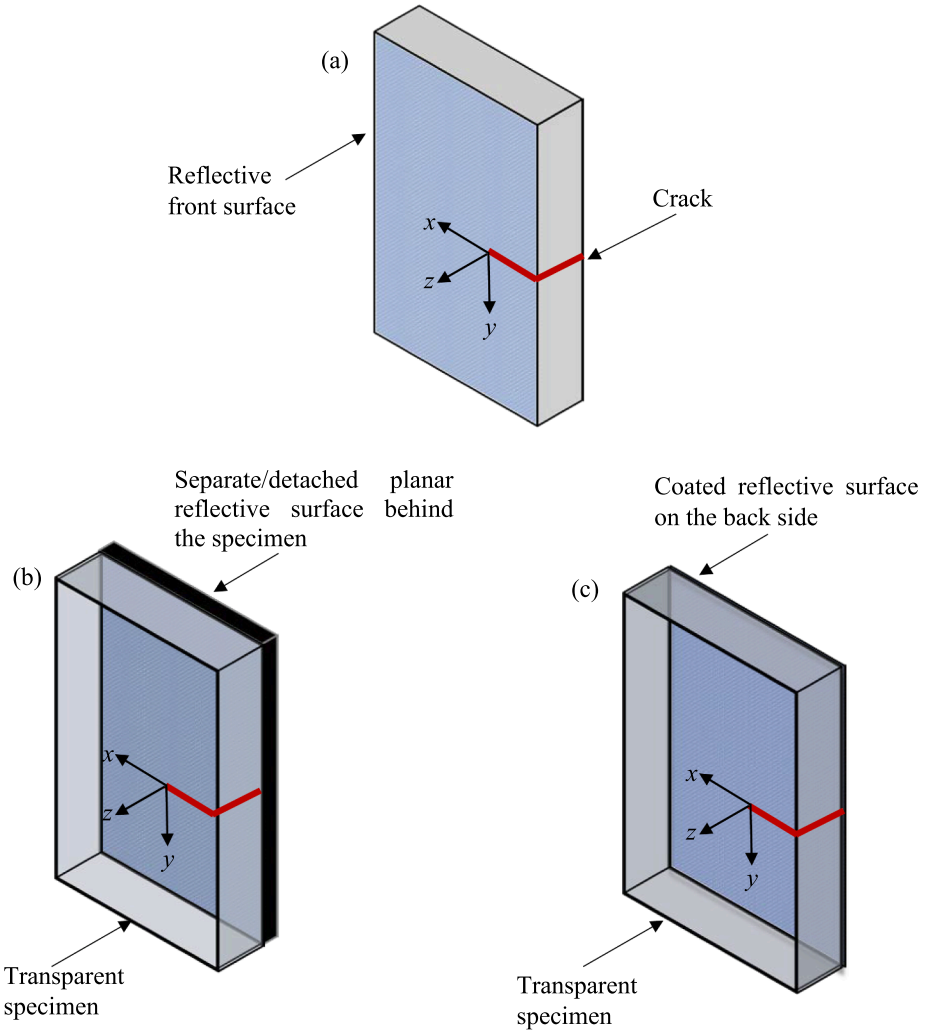

Fig. 2. Specimen configurations for: (a) *r*-DGS; (b) *t2*-DGS; (c) *tr*-DGS [18].

2.3. Double-transmission Digital Gradient Sensing (t2-DGS)

A schematic of the experimental setup for *double-transmission* Digital Gradient Sensing or simply *t2*-DGS method is similar to the one shown in Fig. 1. That is, it has a setup similar to that for *r*-DGS (Fig. 2(a)) except a reflective planar surface is placed flush with the specimen on its backside, as shown in Fig. 2(b). (Or, the gap between the additional reflective surface and the rear surface of the specimen is nominally zero.) The light rays, originating from the target plane, pass through the transparent specimen and reach the reflective surface and then get reflected back into the transparent specimen. Hence, the speckles on the target are recorded by the camera via the added reflective surface. As in *r*-DGS, a reference image is recorded first and then the images in the deformed state as the specimen is subjected to load. The local displacements $\delta_{y:x}$ are then measured by correlating the reference speckle image with those in the deformed state. Thus, light rays experience the elasto-optical effects over twice the specimen thickness as a result of *retro*-reflection. Hence, the two orthogonal stress gradients measured by *t2*-DGS can be related to $\phi_{y:x}$ as [18],

$$(\phi_{y:x})_{t2-DGS} = \frac{\delta_{y:x}}{\Delta} = 2C_\sigma B \frac{\partial(\sigma_{xx} + \sigma_{yy})}{\partial(y\colon x)} \tag{3}$$

where C_σ is the elasto-optic constant of the specimen material, B is the undeformed thickness.

2.4. Transmission-Reflection Digital Gradient Sensing (tr-DGS)

The schematic of the experimental setup for *transmission-reflection* Digital Gradient Sensing (*tr*-DGS) method is also similar to the one shown in Fig. 1. Furthermore, the experimental setup for *tr*-DGS is akin to the one for *t2*-DGS. However, in *tr*-DGS, the specimen is transparent but its rear face is made reflective by depositing a reflective film, as shown in Fig. 2(c). The light rays, originating from

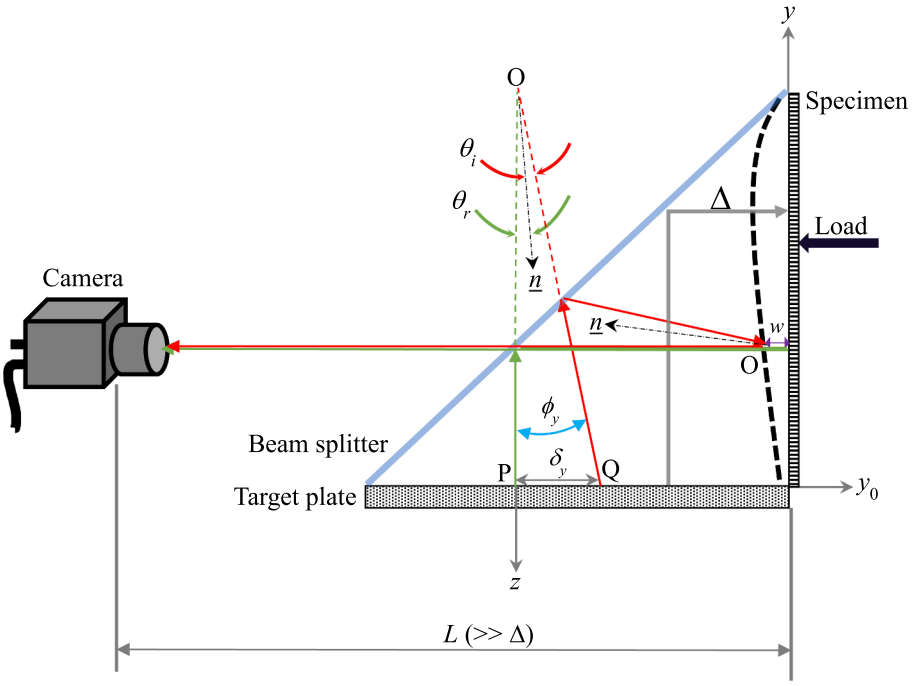

Fig. 3. Working principle of *r*-DGS [18].

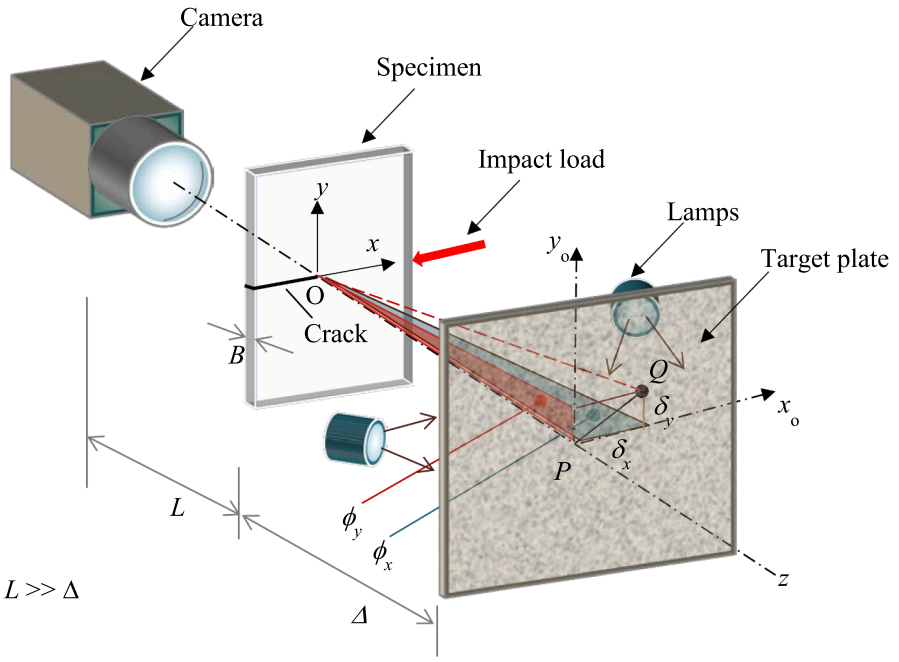

Fig. 4. Schematic of experimental setup for *t*-DGS [13].

the target plane, pass through the transparent specimen and then reflected at its rear surface. The reflected rays then propagate through the transparent specimen for a second time. As in other DGS methods, a reference image is recorded first followed by images in the deformed state of the specimen. That is, gray scale at point P on the target plate which corresponds to point O on the specimen plane is recorded by a pixel of the camera sensor. In addition to the refractive index and thickness changes of the specimen, in this case the reflective rear surface of the specimen also suffers deformation due to stress. As a result of these combined effects, light rays deviate from their initial path. In the deformed state of the specimen, an image is recorded. That is, the gray scale at a neighboring point of P, namely Q on the target plane, is recorded through O on the specimen plane by the same pixel of the camera sensor. As

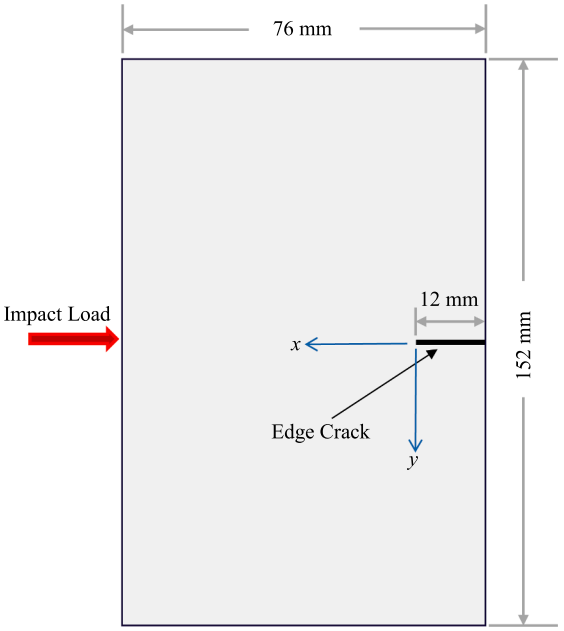

Fig. 5. Specimen geometry and loading configuration.

before, the local speckle displacements $\delta_{x:y}$ can be quantified by correlating the reference image with those in the deformed state of the specimen.

In *r*-DGS, the reflective (front) surface deforms when the specimen is stressed. In *t2*-DGS, the refractive index and thickness of the specimen change when the specimen is stressed. The *tr*-DGS method combines *r*-DGS and *t2*-DGS. That is, in *tr*-DGS, the refractive index and thickness of the specimen change, and the reflective rear surface of specimen also deforms when the specimen is stressed, which makes *tr*-DGS significantly more sensitive for the same stress field as these effects are additive in nature. Hence, the angular deflections of light rays of *tr*-DGS $(\phi_{x:y})_{tr-DGS}$ is a combination of *r*-DGS $(\phi_{x:y})_{r-DGS}$ and *t2*-DGS $(\phi_{x:y})_{t2-DGS}$ [18],

$$(\phi_{x:y})_{tr-DGS} = \frac{\delta_{x:y}}{\Delta} = \left(2C_\sigma B - \frac{\upsilon B}{E}\right)\frac{\partial(\sigma_{xx} + \sigma_{yy})}{\partial(x{:}\ y)} \tag{4}$$

where C_σ is the elasto-optic constant of the specimen material, B is the undeformed thickness, υ is the Poisson's ratio, and E is the elastic modulus of the specimen material.

In light of the above, the measurement sensitivity of *t2*-DGS higher than *r*-DGS by $\left(-\frac{2EC_\sigma}{\upsilon}\right)$, and *tr*-DGS by $\left(1 - \frac{2EC_\sigma}{\upsilon}\right)$. Assuming nominal values of material parameters of soda-lime glass as $E = 70$ GPa, $\upsilon = 0.22$ and $C_\sigma = -2.7 \times 10^{-12}$ m^2/N, the *magnitudes* of these factors are 1.72 and 2.72, respectively.

3. *r*-DGS measurements

The *reflection* DGS (*r*-DGS) was first applied to study dynamic fracture of soda-lime glass plates. Single edge notched (SEN) specimens of dimensions 152 mm × 76 mm, as shown in Fig. 5, were cut from a 9.5 mm thick sheet stock. An initial notch of 12 mm length was cut at the middle of the long edge using a 300 μm thick diamond impregnated circular saw. An impact load was also imposed at the middle of the edge opposite to the cracked edge. One of the two 152 mm × 76 mm faces of the specimen was made reflective by depositing aluminum film to implement *r*-DGS.

The schematic of the experimental setup used is shown in Fig. 6. A modified Hopkinson pressure bar, or simply a 'long-bar', was used for loading the edge cracked specimen. The long-bar was a 1.83 m steel rod of 25.4 mm diameter with a polished wedge-shaped tip for impacting an unconstrained glass plate on the edge opposite to the cracked edge. A 305 mm long, 25.4 mm diameter steel striker placed in the barrel of a gas-gun was co-axially aligned with the long-bar at the start of the experiment. The striker was launched towards the long-bar at a velocity of approx. 4 m/s during tests. A close-up of the optical arrangement is also shown in Fig. 6. Initially, the long-bar tip was kept in contact with the specimen. The specimen was positioned on a height-adjustable platform using a ~ 1.5 mm thick rectangular soft putty strip to prevent direct contact with the platform. To achieve symmetry in terms of acoustic impedance relative to the loading axis, another identical putty strip was pressed onto the top edge of the specimen. The putty strips isolated the specimen from the platform to create an approximately 'free surface' conditions except on the loading faces. A beam splitter and the speckle target plate were placed in a 45° holder so that the camera could be focused on the speckles through the beam splitter via the reflective specimen surface. The speckle images were photographed by a Kirana-05 M ultrahigh-speed digital camera with a single, fixed-resolution sensor capable of recording 180, 10-bit gray scale images at a maximum rate of 5 million

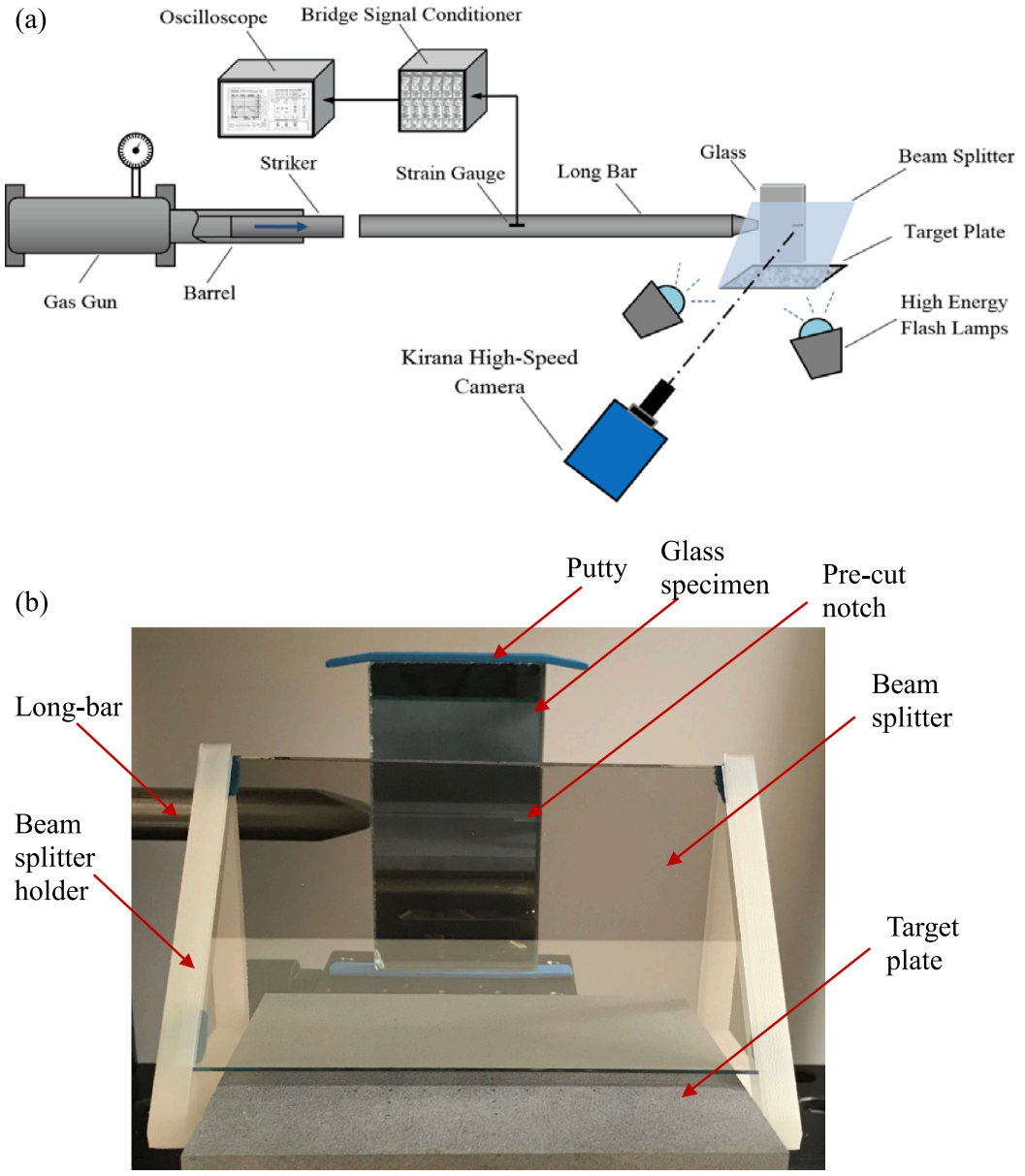

Fig. 6. Schematic (top) and close-up photograph (bottom) of the experimental setup used to study dynamic fracture of soda-lime glass.

frames per second and spatial resolution of 924 × 768 pixels per image. The speckles on the target plate were illuminated using a pair of Cordin-659 high energy flash lamps.

A Sigma 150–600 mm focal length zoom lens with an adjustable bellows was used with the camera to record the speckle images from a long distance. The distance between the specimen and the lens plane (L) was ~ 1600 mm and the one between the specimen mid-plane and the target plane (Δ) was ~ 700 mm. With these settings, the camera recorded information from a rectangular region of approximately 40 mm × 50 mm on the specimen plane in the vicinity of the pre-notch tip as the region-of-interest (ROI). When the long-bar was impacted by the striker, a compressive stress wave propagated the entire length of the bar. A trigger pulse was also generated at the moment of impact to start recording the speckle images by the camera with a prescribed delay. A total of 180 images, some in the undeformed state and others in the deformed state of the specimen, were recorded at 1,000,000 frames per second (inter frame period 1 μs). An image just before the start of deformation was selected as the reference image. Subsequent images corresponding to the deformed state were correlated with the reference image using ARAMIS® image analysis software. During analysis, a sub-image size of 30 × 30 pixels (1 pixel = 76.88 μm on the specimen) with 25 pixels overlap was used to extract the local displacements $\delta_{x;y}$ in the ROI. The displacement fields were then used to compute the two orthogonal surface slopes, $\frac{\partial w}{\partial x;y}$ where w is the local out-of-plane displacement.

The time-resolved angular deflection contour plots of $\phi_{x;y}$ ($\approx 2\frac{\partial w}{\partial x;y}$) around a dynamically loaded mode-I crack in the glass plate

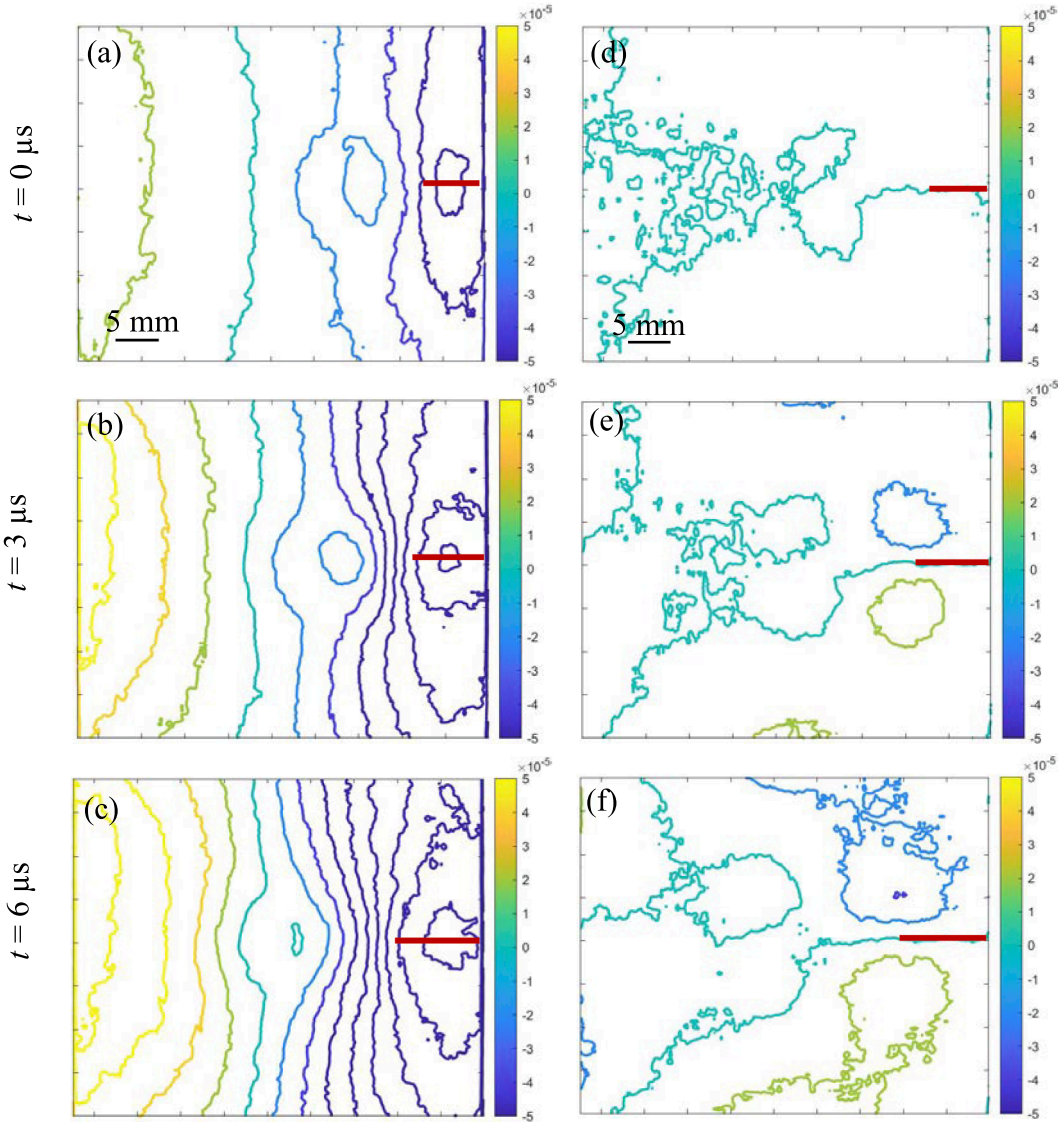

Fig. 7. Measured angular deflection contours ϕ_x (left column) and ϕ_y (right column) near a mode-I crack in soda-lime glass plate using *r*-DGS. Top row corresponds to crack initiation and the bottom two for a growing crack. Contour increment = 20×10^{-6} rad. Red stripes highlight the crack.

are shown in Fig. 7 at a few select time instants. In these plots, $t = 0\ \mu s$ corresponds to crack initiation at the original notch-tip. It can be observed that, due to the symmetric nature of mode-I fracture, the crack propagates self-similarly along a horizontal path (from right to left in these images) and hence the contours of the two orthogonal surface slopes are generally symmetric in shape relative to the initial crack. The contours near the left-hand edge in these plots are attributed to the stress concentration due to the impact load on that edge (outside the ROI). When compared to the angular deflection contours around a mode-I crack in other materials measured by *r*-DGS [20,21], the singular nature of the crack-tip field is not evident in these contours. That is, the contours do not seem to converge to a single point corresponding to the crack tip. This is because, the out-of-plane deformation around the crack-tip in soda-lime glass plate is expected to be less than 100 nm (negative), and such a small out-of-plane deformation was essentially drowned out by the positive out-of-plane deformations at the impact point on the left side of the specimen. As a result, the out-of-plane deformation contours around the crack tip appear relatively diffuse, without a point of convergence at the crack tip. Hence, DGS methods of higher measurement sensitivity are needed to study dynamic fracture of stiff and low-toughness materials.

4. *t2*-DGS And *tr*-DGS measurements

Next, two modified DGS methods, *t2*-DGS and *tr*-DGS, with higher measurement sensitivity [18] than *r*-DGS but experimental setups similar to that for *r*-DGS were used to study dynamic crack growth in soda-lime glass. The specimen geometry and loading configuration were also same. A close-up of the optical arrangement for *t2*-DGS is shown in Fig. 8 where a planar reflective mirror

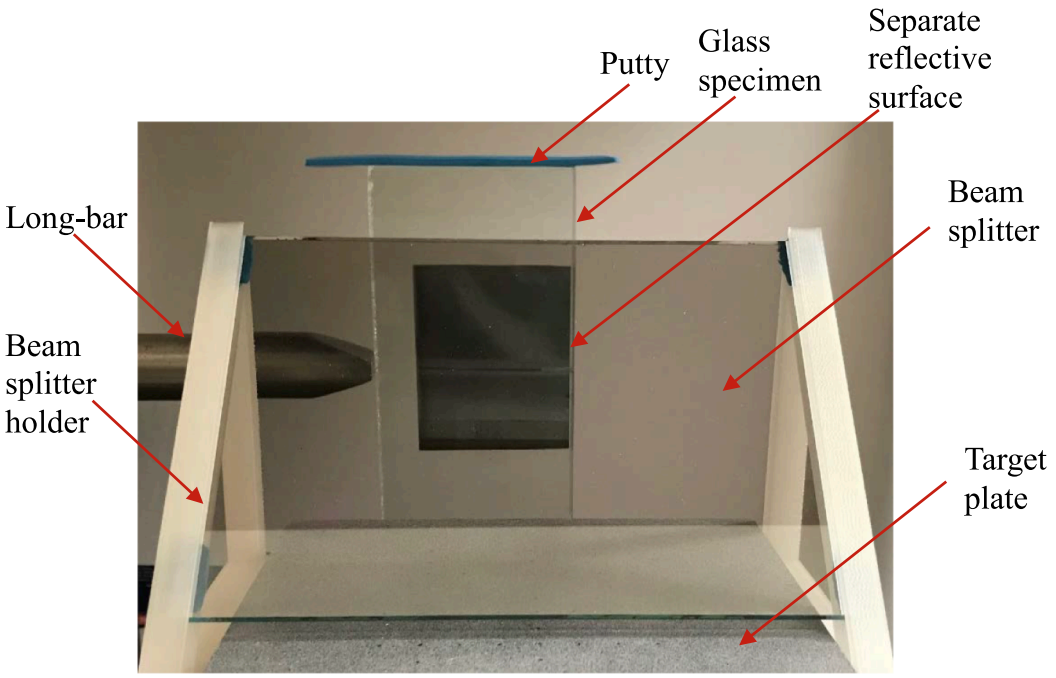

Fig. 8. Close-up photograph of experimental setup for *t2*-DGS.

placed flush with the soda-lime glass specimen on its backside can be seen. For *tr*-DGS, the back surface of specimen was made reflective by depositing aluminum film on it using vapor deposition technique. The distance between the specimen and the lens plane (L) was ~ 1300 mm and the one between the specimen and the target plane (Δ) was ~ 200 mm for both *t2*-DGS and *tr*-DGS. Note that Δ used for *t2*- and *tr*-DGS were significantly shorter than the one used for *r*-DGS (~700 mm).

A few select time-resolved angular deflection contour plots of $\phi_{x;y}$ around a dynamically loaded mode-I crack measured by *t2*-DGS and *tr*-DGS are shown in Fig. 9 and Fig. 10, respectively. In these plots, $t = 0\ \mu s$ corresponds to crack initiation at the original notch-tip. It can be observed that contours are rather well-defined and converge to the crack tip unlike those in Fig. 7. This indicates that the higher sensitivity of *t2*-DGS and *tr*-DGS relative to *r*-DGS are helpful for visualizing the singular nature of the crack-tip field quantitatively in soda-lime glass plates. The contour plots in both Fig. 9 and Fig. 10 are plotted with the same contour increment of 20 micro-radians. When compared to the contours measured using *t2*-DGS in Fig. 9, those measured by *tr*-DGS in Fig. 10 are larger in size and denser, consistent with the higher sensitivity of *tr*-DGS relative to *t2*-DGS.

The contours of $(\sigma_x + \sigma_y)$ computed by 2D integration of stress gradients data from *t2*-DGS in conjunction with Higher-order Finite-difference-based Least-squares Integration (HFLI) algorithm [22] are plotted in Fig. 11. It is evident that the singular crack-tip stresses before crack initiation and during crack growth are tensile and expected. As noted earlier in the context of *r*-DGS results, the compressive stresses are negative on the left side edge of the specimen and are attributed to impact loading.

The crack velocity histories for four different experiments, two specimens each for *t2*-DGS and *tr*-DGS, obtained from the respective angular deflection contours are shown in Fig. 12. It can be observed that the velocity histories for all the specimens overlap on each other, indicating good repeatability of measurements between *t2*-DGS and *tr*-DGS methods. The velocity histories increase from 0 to ~ 1300 m/s in 3–4 μs after crack initiation and then, apart from small fluctuations in the histories, they become rather steady at ~ 1400 m/s. This is consistent with velocity observations for soda-lime glass made by Sundaram and Tippur [15] using *t*-DGS method.

The micrographs of fracture surface produced by crack growth are shown in Fig. 13. It shows the mirror-mist-hackle zones, again consistent with those reported by other investigators [23]. The mirror region is observed first at the early stages of crack growth, soon after crack initiation from the initial notch. The arc shaped marks, known as Wallner lines due to interference of stress waves emanating from the crack tip and reflected stress waves from the free surfaces, can be seen in the mirror region. After the crack grows for a certain distance, the mirror regions transitions to mist region due to increased surface roughness can be observed. The mist region is followed by the hackle region, where the fracture surface is visibly rough. When examined relative to Fig. 12, the steady crack velocities occur in the mirror region, and then the fluctuations of crack velocities occur in the mist and hackle regions.

The stress intensity factor (SIF) histories were evaluated using an over-deterministic least-squares analysis based on the angular deflection fields of (ϕ_x) measured by *tr*-DGS and *t2*-DGS methods and asymptotic mechanical field description,

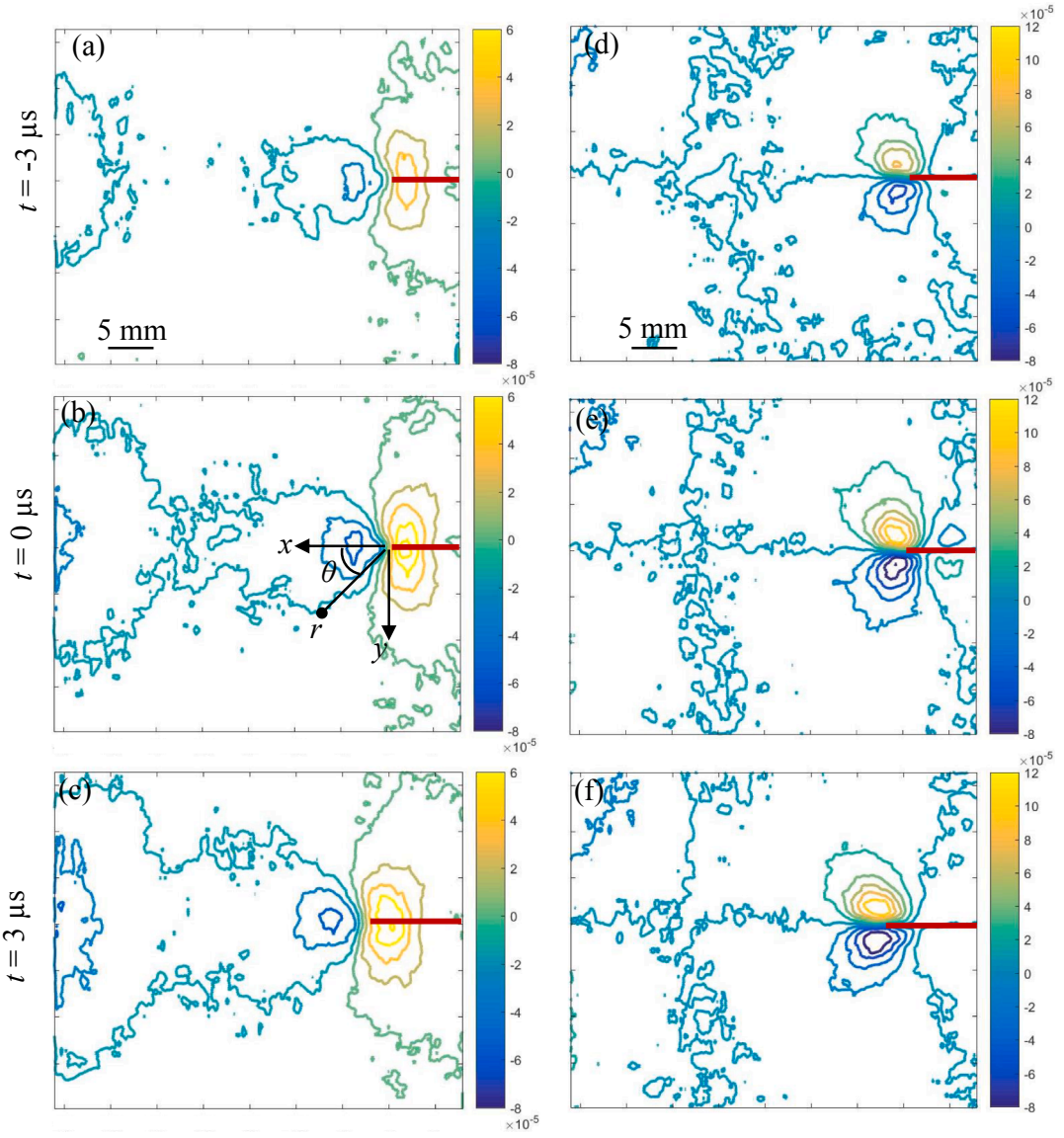

Fig. 9. Measured angular deflection contours ϕ_x (left column) and ϕ_y (right column) for dynamic fracture of glass using *t2*-DGS. t = 0 corresponds to crack initiation; Contour increment = 20×10^{-6} rad. Red stripes represent the crack.

$$\phi_x(t) = D\left[\begin{array}{l} -\frac{1}{2}r^{-\frac{3}{2}}\left\{\begin{array}{l} f(V;C_L;C_S)A_1(t)\cos\left(\frac{3\theta}{2}\right) \\ +g(V;C_L;C_S)D_1(t)\sin\left(-\frac{3\theta}{2}\right)\end{array}\right\} \\ +\sum_{N=2}^{\infty}\left(\frac{N}{2}-1\right)r^{\left(\frac{N}{2}-2\right)}\left\{\begin{array}{l} A_N(t)\cos\left(\left(\frac{N}{2}-2\right)\theta\right) \\ +D_N(t)\sin\left(\left(\frac{N}{2}-2\right)\theta\right)\end{array}\right\}\end{array}\right] \quad (5)$$

where the constant D varies for each of the DGS methods, $D_{t2-DGS} = (2C_\sigma B)$ and $D_{tr-DGS} = \left(2C_\sigma B - \frac{\upsilon B}{E}\right)$, C_σ is the elasto-optic constant of soda-lime glass (-2.7×10^{-12} m^2/N), B is its initial thickness, E and υ are elastic modulus and Poisson's ratio, respectively. The functions f and g are dependent on instantaneous crack velocity, (r, θ), as shown in Fig. 9(b), denotes the contracted crack-tip polar coordinates for a growing crack, $r = \{(x)^2 + \alpha_L{}^2(y)^2\}^{1/2}$ and $\theta = \tan^{-1}\left(\frac{\alpha_L y}{x}\right)$. The mode-I and mode-II SIFs $K_I(t)$ and $K_{II}(t)$ are related to the coefficients of $A_1(t)$ and $D_1(t)$, respectively, as $A_1(t) = K_I(t)\sqrt{2/\pi}$ and $D_1(t) = K_{II}(t)\sqrt{2/\pi}$. The values of (ϕ_x) measured by *t2*-DGS and *tr*-DGS were used to calculate the two SIFs. The functions f and g are [22],

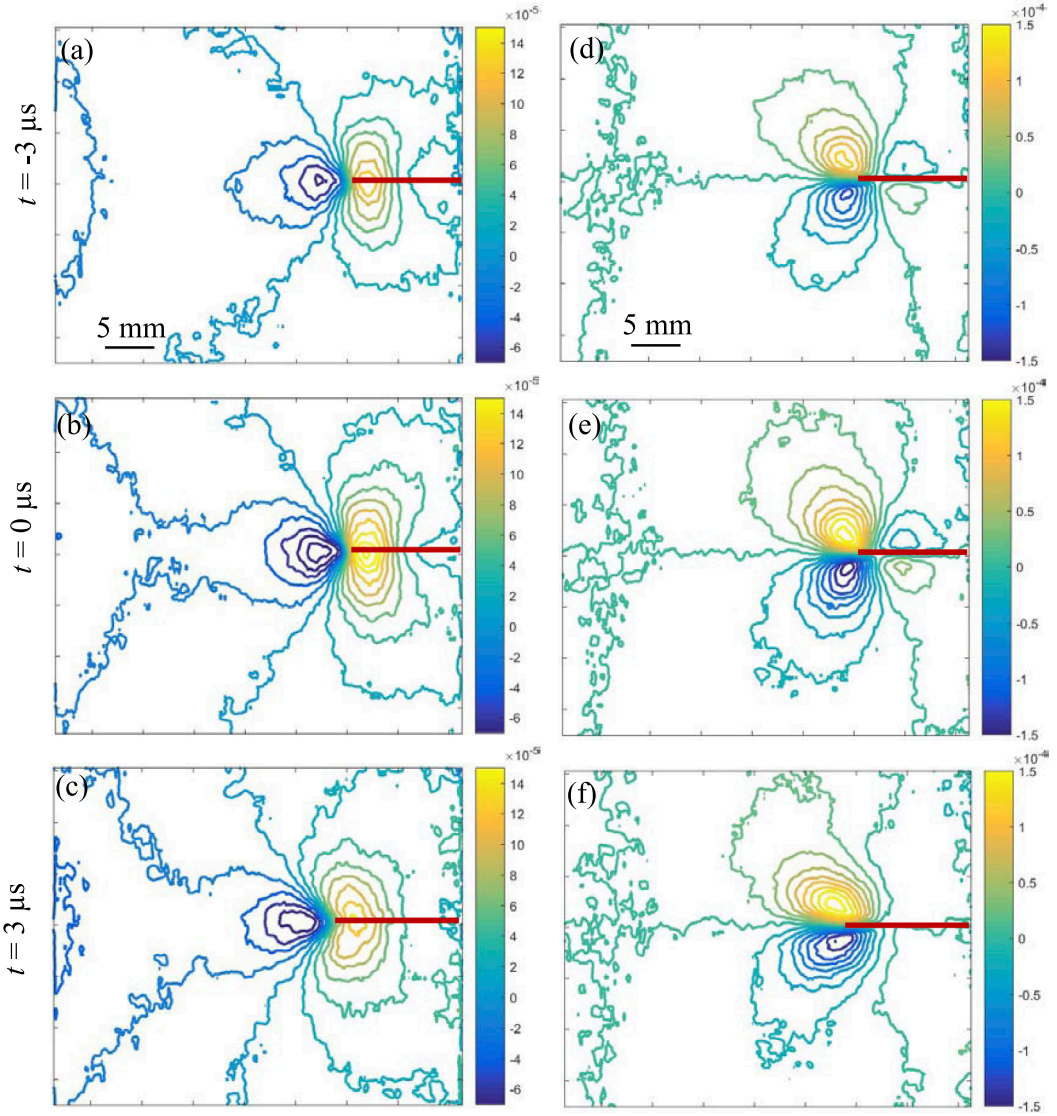

Fig. 10. Measured angular deflection contours ϕ_x (left column) and ϕ_y (right column) for dynamic fracture of glass using *tr*-DGS. t = 0 corresponds to crack initiation; Contour increment = 20×10^{-6} rad. Red stripes represent the crack.

$$f(V; C_L, C_S) = \left(\frac{1+\upsilon}{1-\upsilon}\right)\frac{(1+\alpha_S{}^2)(1-\alpha_L{}^2)}{4\alpha_L\alpha_S - (1+\alpha_S{}^2)^2}$$

$$g(V; C_L, C_S) = \left(\frac{1+\upsilon}{1-\upsilon}\right)\frac{2\alpha_S(1-\alpha_L{}^2)}{4\alpha_L\alpha_S - (1+\alpha_S{}^2)^2} \tag{6}$$

where $\alpha_L = \left[1 - \frac{\rho(1-\upsilon)}{2\mu}V^2\right]^{\frac{1}{2}}$ and $\alpha_S = \left[1 - \frac{\rho}{\mu}V^2\right]^{\frac{1}{2}}$ for plane stress. The ϕ_x field data in the region around the crack-tip, $0.4 \le r/B \le 1.0$, $-140^\circ \le \theta \le 140^\circ$, were utilized in the regression analysis. The effect of the non-singular far-field deformations on the measured K_I and K_{II} was offset by using four higher order terms ($N = 4$) in Eq. (5).

To complement the measurements, an elasto-dynamic 3D finite element model was simulated using ABAQUS® structural analysis software and SIF history prior to crack initiation was evaluated independently. The numerical model contained part of the long-bar and the entire single edge notched specimen (152 mm × 76 mm × 9.5 mm) to simulate stress wave propagating into the specimen. The long-bar was 50.8 mm long in the model with a 6.3 mm × 25.4 mm rectangular face in contact with the specimen as in the experiment. A kinematic contact conditions was adopted between the long-bar and the specimen for simulating dynamic loading. The material properties of the specimen and the long-bar used in the simulation are shown in Table 1. The entire 3D model consisted of 71,775 and 679,174 modified 10-node tetrahedral elements for the long-bar and the specimen, respectively. The discretization in regions around the impact location and the crack tip were highly refined with elements of size 0.1 mm. The discretized model along

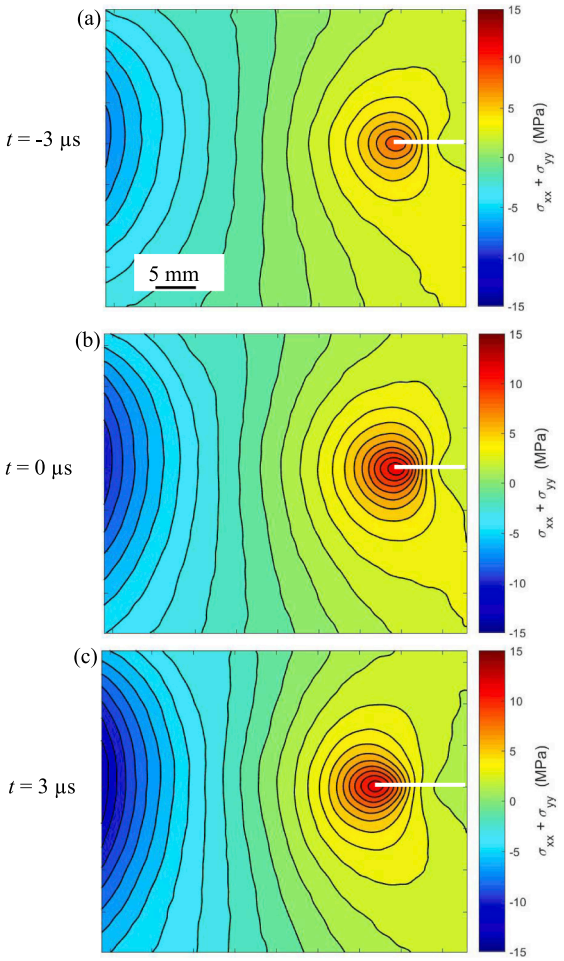

Fig. 11. Contours of $(\sigma_x+\sigma_y)$ obtained by integrating stress gradient fields from *t2*-DGS shown in Fig. 9 using HFLI [22]. Contour increment = 1 MPa. White stripes highlight the crack.

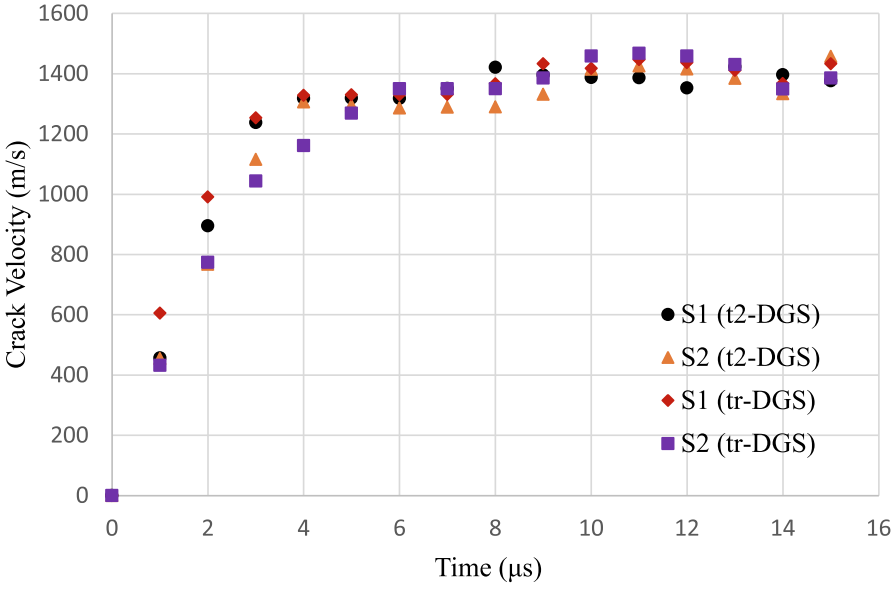

Fig. 12. Crack velocity histories for four different specimens from nominally identical loading using *t2*-DGS and *tr*-DGS.

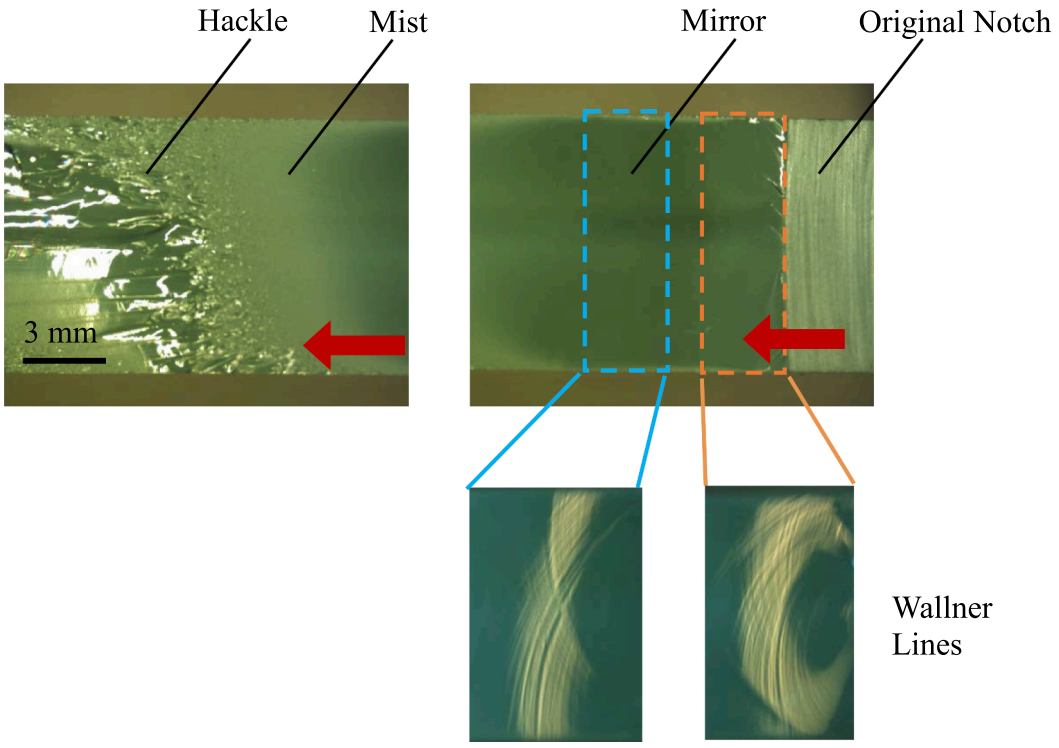

Fig. 13. Fractography showing 'mirror', 'mist', and 'hackle' features on a fractured soda-lime glass specimen. Red arrows show crack propagation direction.

Table 1
Material properties of maraging steel and soda-lime glass used in the simulation.

Properties	Soda-lime Glass	Maraging Steel
E (GPa)	70	200
υ	0.22	0.3
ρ (Kg/m^3)	2500	8000

with the crack opening displacement contours is shown in Fig. 14(a). The symmetry of these contours about the crack plane are consistent with the mode-I deformations expected from this simulation. Fig. 14(b) shows the strain history measured using the strain gage on the long-bar during an experiment. The particle velocity history calculated from the strain history, $V_p = c\varepsilon$ (where c is the bar wave speed in steel and ε is the measured strain on the bar), was used as input to the simulation. The apparent mode-I and mode-II SIFs, $(K_{I;II})_{app}$, at each time step were calculated from the instantaneous crack opening (v) and sliding (u) displacements extracted along the two crack faces using [17]:

$$(K_{I;II})_{app} = \frac{E\sqrt{2\pi}}{8\sqrt{r}}(v;\, u);\ (r,\, \theta = \pi) \tag{7}$$

The instantaneous values of $(K_{I;II})$ were determined by extrapolating the linear portion of $(K_{I;II})_{app}$ plotted as a function of the radial distance r along $\theta = \pi$.

The SIFs obtained from Eq. (5) and finite element computations are plotted in Fig. 15. Two specimens were studied using each of the optical methods. The time axis of each plot was shifted so that $t = 0$ corresponds to crack initiation at the original crack-tip. The solid and open symbols in Fig. 15 represent K_I and K_{II}, respectively. The agreement of the SIFs between all the specimens indicates good experimental repeatability and measurement consistency from the two optical methods used. The finite element results match the experimental counterparts very well. The K_I histories increase monotonically until crack initiation for all specimens. The dynamic fracture toughness (K_I at $t = 0$) was recorded as 0.78 ± 0.02 MPa m$^{1/2}$. The time rate of change of K_I, or $\frac{dK_I}{dt}$, was calculated as ~ (7.4 ± 1.1) × 10^4 MPa m$^{1/2}$/s at crack initiation from a few data points in the K_I history leading up to initiation. A noticeable drop in the K_I histories after crack initiation, to ~ 0.65 MPa m$^{1/2}$, can be observed and is attributed to dynamic unloading at crack initiation from the notch. It should be noted that this value of K_I corresponds to a mathematically sharp crack initiated from the notch tip characterizing the crack initiation toughness. Subsequently, K_I histories become relatively constant in the mirror phase of crack growth. The apparent K_I histories then increase monotonically again until the end of the observation window as (a) the crack

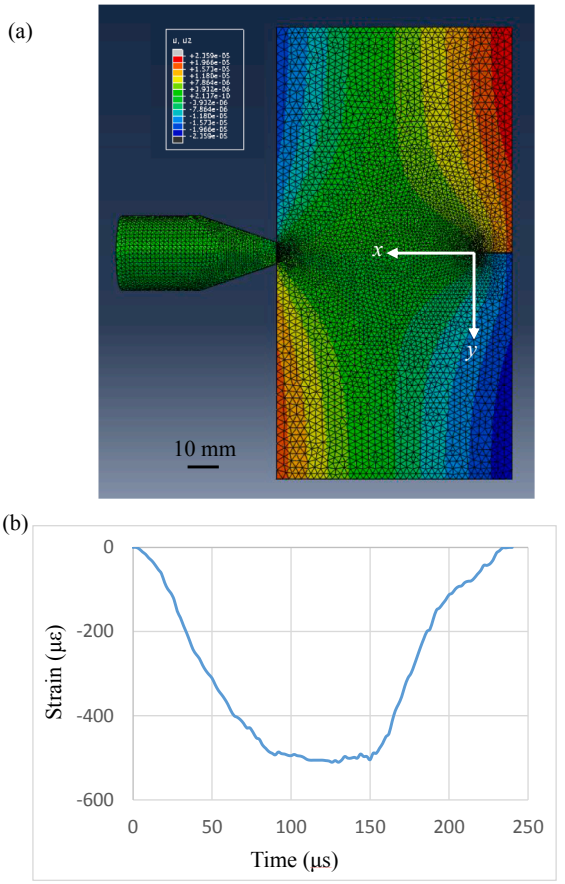

Fig. 14. (a) Discretized finite element grid superposed with crack opening displacement contours. (b) The strain history from the compressive stress pulse measured using the strain gage on the Hopkinson bar.

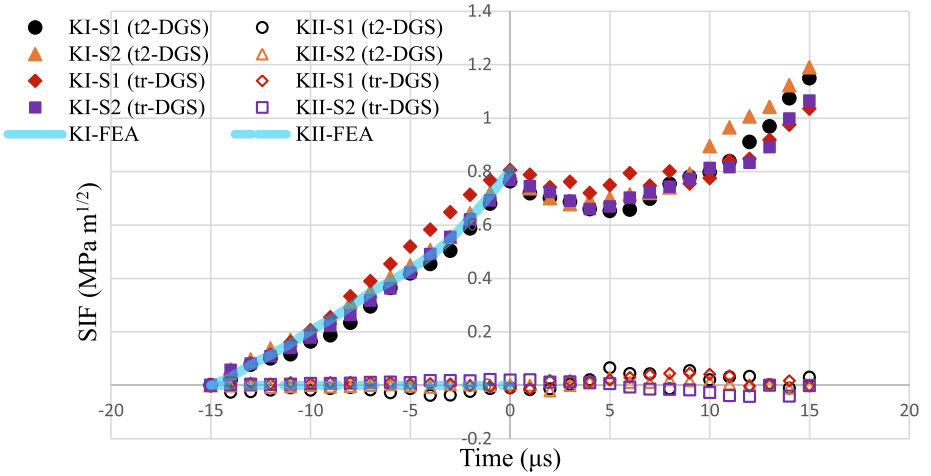

Fig. 15. Stress intensity factor histories measured by t2-DGS and tr-DGS methods, and finite element analysis prior to crack initiation. t = 0 corresponds to crack initiation.

propagated towards the compression dominated region of the specimen due to the impact on its left edge, (b) the crack propagation consumed more energy as the roughness of crack surface increased in the mist and hackle zones seen in Fig. 13. The apparent K_{II} histories throughout the window are nearly zero, in both the pre- and post-crack initiation regimes, due to the mode-I nature of fracture. The nonzero values of K_{II} suggest potential errors in the least-squares analysis employed and crack tip location during data analysis.

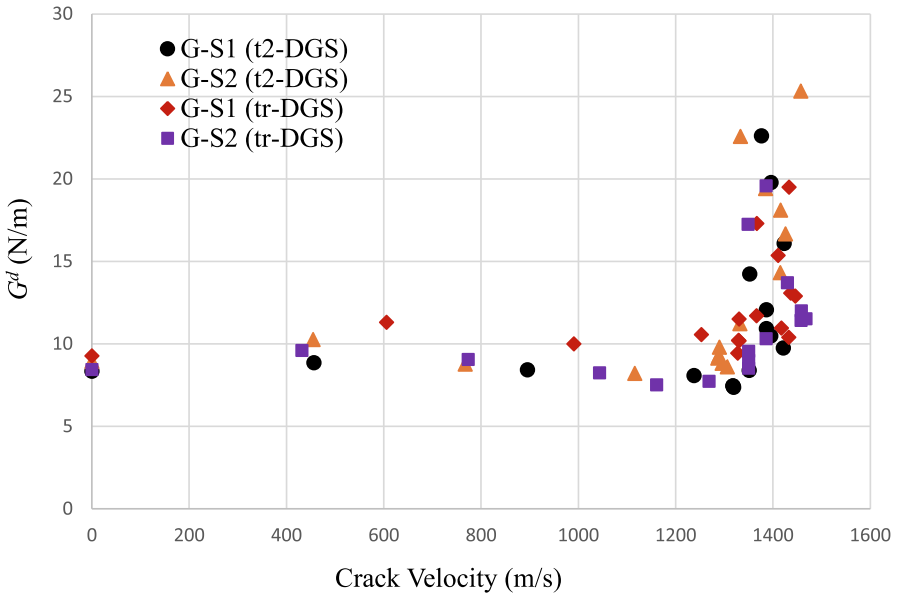

Fig. 16. Variation of dynamic strain energy release rates (G^d) with crack velocity (V) from four different nominally identical soda-lime glass experiments.

The dynamic energy release rates for growing cracks were calculated from the measured crack velocities, V, and SIFs shown in Fig. 12 and Fig. 15, respectively, using [24]:

$$G^d = \frac{1}{E}[A_I(V)K_I^2 + A_{II}(V)K_{II}^2] \tag{8}$$

where $A_I(V) = \frac{V^2\alpha_L}{(1-\nu)C_s^2 D}$, $A_{II}(V) = \frac{V^2\alpha_s}{(1-\nu)C_s^2 D}$, with $C_s = \sqrt{\frac{\mu}{E}}$ being the shear wave speed, and $D = 4\alpha_L\alpha_s - (1+\alpha_s^2)^2$. The plot of dynamic strain energy release rates (G^d) with crack velocity (V) is shown in Fig. 16. It can be observed that the measured G^d is ~ 8.8 N/m at the crack initiation. Initially G^d is nearly a constant, ranging between ~ 9 to ~ 7.5 N/m (J/m^2), until crack velocity reaches ~ 1300 m/s. Subsequently, the G^d values rapidly increase to ~ 25 N/m in a narrow velocity range of 1350–1450 m/s. Despite plotting two independently measured quantities relative to each other, a good agreement between different measurements indicates consistency of results from these two optical methods.

5. Conclusions

Two modified DGS methods with significantly higher measurement sensitivity have been shown to allow visualization and quantification of two orthogonal stress gradient fields around the crack-tip in single-edge-notched soda-lime glass plates subjected to dynamic impact loading. The measured stress gradients fields were also integrated numerically using HFLI algorithm to obtain ($\sigma_{xx} + \sigma_{yy}$) stress fields in the ROI. The higher measurement sensitivities of both *t2*-DGS and *tr*-DGS were very attractive to detect the stress gradients around mathematically sharp crack-tip in this high-stiffness and low-toughness material without using a relatively large target distance, and hence errors due to thermal currents in the optical path and vibration could be mitigated relative to traditional *r*-DGS and *t*-DGS methods without any sensor exposure issues. By employing ultrahigh-speed photography at 1 Mfps, the growing crack was clocked at ~ 1400 m/s during steady state conditions. The stress intensity factor histories were also calculated during pre- and post-crack initiation regimes. The dynamic fracture toughness at crack initiation was recorded as 0.78 ± 0.02 MPa m$^{1/2}$ from the notch tip and ~ 0.65 MPa m$^{1/2}$ after accounting for unloading. The dynamic strain energy release rates, G^d, were also extracted and plotted as a function of measured crack velocity. The plot shows a rapid increase in G^d values from ~ 9 to ~ 25 N/m when the crack reached ~ 1400 m/s. The results obtained from *t2*-DGS and *tr*-DGS matched with each other across multiple specimens indicating good measurement consistency in these two optical methods. The good match between the results obtained from experiments and finite element simulations supplement the results further supporting these two optical methods for studying dynamic fracture mechanics of this challenging material.

Declaration of Competing Interest

The authors declare that they have no known competing financial interests or personal relationships that could have appeared to influence the work reported in this paper.

Acknowledgments

Partial support for this research through Army Research Office grants W911NF-16-1-0093 and W911NF-15-1-0357 (DURIP) are gratefully acknowledged.

References

[1] Patel PJ, Glide GA, Dehmer PG, McCauley JW. Transparent Armor. New York: AMPTIAC Newsletter; 2000.
[2] Bourne NK, Rosenberg Z, Mebar Y, Obara T, Field JE. A high-speed photographic study of fracture wave propagation in glasses. Journal De Physique IV Colloque 1994;04:C8635–40.
[3] Park H, Chen WW. Experimental Investigation on dynamic crack propogating perpendicular through interface in glass. J Appl Mech 2011;78.
[4] McCauley J, Strassburger E, Patel P, Paliwal B, Ramesh K. Experimental observations on dynamic response of selected transparent armor materials. Exp Mech 2013;53:3–29.
[5] Swab JJ, Meredith CS, Casem DT, Gamble WR. Static and dynamic compression strength of hotpressed boron carbide using a dumbbell-shaped specimen. J Mater Sci 2017;52:10073–84.
[6] Parab ND, Guo Z, Hudspeth MC, Claus BJ, Fezzaa K, Sun T, Chen WW. Fracture mechanisms of glass particles under dynamic compression. Int J Impact Engng 2017;106:146–54.
[7] Leong AFT, Robinson AK, Fezzaa K, Sun T, Sinclair N, Casem DT, Lambert PK, Hustedt CJ, Daphalapurkar NP, Ramesh KT, Hufnagel TC. Quantitative In Situ Studies of Dynamic Fracture in Brittle Solids Using Dynamic X-ray Phase Contrast Imaging. Exp Mech 2018;58:1423–37.
[8] Dally J. Dynamic photoelastic studies of fracture. Exp Mech 1979;10:349–61.
[9] Tippur HV, Krishnaswamy S, Rosakis AJ. A coherent gradient sensor for crack tip deformation measurements: analysis and experimental results. Int J Fract 1991;48:193–204.
[10] Zhang QB, Zhao J. Effect of loading rate on fracture toughness and failure micromechanisms in marble. Engng Fract Mech 2013;102:288–309.
[11] Ju M, Li J, Yao Q, Li X, Zhao J. Rate effect on crack propagation measurement results with crack propagation gauge, digital image correlation, and visual methods. Engng Fract Mech 2019;219.
[12] Shannahan L, Barsoum MW, Lamberson L. Dynamic fracture behavior of a MAX phase Ti3SiC2. Engng Fract Mech 2017;169:54–66.
[13] Periasamy C, Tippur HV. Full-field digital gradient sensing method for evaluating stress gradients in transparent solids. Appl Opt 2012;51(12):2088–97.
[14] Periasamy C, Tippur HV. A full-field reflection-mode digital gradient sensing method for measuring orthogonal slopes and curvatures of thin structures. Meas Sci Technol 2013;24.
[15] Sundaram BM, Tippur HV. Full-field measurement of contact-point and crack-tip deformations in soda-lime glass. Part-II: Stress wave loading. Int J Appl Glass Sci 2018;9:123–36.
[16] Dondeti S, Tippur HV. A Comparative Study of Dynamic Fracture of Soda-Lime Glass Using Photoelasticity, Digital Image Correlation and Digital Gradient Sensing Techniques. Exper Mech 2019:1–17.
[17] Periasamy C, Tippur HV. Measurement of crack-tip and punch-tip transient deformations and stress intensity factors using Digital Gradient Sensing technique. Engng Fract Mech 2013;98:185–99.
[18] Miao C, Tippur HV. Higher sensitivity Digital Gradient Sensing configurations for quantitative visualization of stress gradients in transparent solids. Opt Lasers Engng 2018;108:54–67.
[19] Tippur HV. Optical Techniques in Dynamic Fracture Mechanics. In: Dynamic Fracture Mechanics, World Scientific Publications; 2006.
[20] Jain AS, Tippur HV. Mapping Static and Dynamic Crack-Tip Deformations Using Reflection-Mode Digital Gradient Sensing: Applications to Mode-I and Mixed-Mode Fracture. J Dynam Behav Mater 2015;1:315–29.
[21] Miao C, Tippur HV. Fracture behavior of carbon fiber reinforced polymer composites: An optical study of loading rate effects. Engng Fract Mech 2019;207:203–21.
[22] Miao C, Sundaram BM, Huang L, Tippur HV. Surface profile and stress field evaluation using digital gradient sensing method. Meas Sci Technol 2016;27.
[23] Sundaram BM, Tippur HV. Dynamic fracture of soda-lime glass: A full-field optical investigation of crack initiation, propagation and branching. J Mech Phys Solids 2018;120:132–53.
[24] Ravi-Chandar K. Dynamic fracture. San Diego: Elsevier; 2004.